Abnormal Strain Rate Sensitivity Driven by a Unit Dislocation-Obstacle Interaction in bcc Fe

Zhitong Bai and Yue Fan*
Department of Mechanical Engineering, University of Michigan, Ann Arbor, Michigan 48109, USA

(Received 25 September 2017; published 22 March 2018)

The interaction between an edge dislocation and a sessile vacancy cluster in bcc Fe is investigated over a wide range of strain rates from 10^8 down to 10^3 s^{-1}, which is enabled by employing an energy landscape-based atomistic modeling algorithm. It is observed that, at low strain rates regime less than 10^5 s^{-1}, such interaction leads to a surprising negative strain rate sensitivity behavior because of the different intermediate microstructures emerged under the complex interplays between thermal activation and applied strain rate. Implications of our findings regarding the previously established global diffusion model are also discussed.

DOI: 10.1103/PhysRevLett.120.125504

Advanced reactors are being designed for longer lifetimes while operating in extreme conditions of temperature and irradiation [1]. The neutron-irradiated ferritic alloys typically include super-saturated defects such as self-interstitial atom and vacancy clusters [2]. The interactions between such defect clusters and dislocations are critical to understand and predict the mechanical degradations of the materials, such as swelling, creep, and embrittlement [3–5].

Negative strain-rate sensitivity (nSRS) is a remarkable phenomenon showing an inverse relation between flow stresses and applied strain rates [6–8], which might lead to detrimental effects such as nonuniform deformation and mechanical instabilities [9]. It is challenging to explain nSRS by the direct interaction between a dislocation and an obstacle. Because according to the classical picture [10], the activation barrier for a local dislocation-obstacle interaction monotonically decreases as stress increases. Two direct implications stem from this picture: (i) the qualitative interaction mechanism is presumably unaffected by surrounding environments; and (ii) only a positive correlation between strain rate and flow stress can be obtained by employing the kinetics theory. Therefore, to explain the nSRS phenomenon, a global diffusion scheme has been proposed: there is an adequate supply of defects that diffuse towards the dislocation, and lower strain rate allows more time for defects concentrate at dislocation core, which yields a stronger resistance and a higher flow stress [9]. Several continuum models have been developed to quantify the nSRS behavior. For example, by assuming the obstacle and dislocation concentrations are time and strain dependent, Estrin *et al.'s* model can predict an inverse behavior if the homogenous nucleation of obstacles in bulk being taken place [11,12]. Curtin *et al's* pioneering work has provided the supporting evidence to such a global diffusion scheme from the fundamental level by investigating the mechanism of a direct single-atomic jump across the dislocation slip plane [13]. In the present work, instead of focusing on global diffusions and concentrations of solutes, we probe a local interaction between a dislocation and a sessile obstacle over a wide range of strain rates, from 10^8 down to 10^3 s^{-1}. We show that the critical resolved shear stress (CRSS) is determined by the complex interplay between thermal activation and the applied strain rate. Because of different intermediate microstructures emerged at various strain rate conditions, a nonmonotonic variation of CRSS and a nSRS at low strain rates have been observed. Such a newly identified mechanism, together with the established global diffusion scheme, might enable a more comprehensive understanding towards the evolutions of irradiated microstructures.

Vacancy clusters or voids are common defects in structural materials and can induce strong resistance to the glide motion of edge dislocation [14]. In this Letter, we therefore consider the interaction between the $1/2\langle 111\rangle$ edge dislocation and a small void containing 9 vacancies in bcc Fe. The simulation system has the dimensions $9.81\ \mathrm{nm}(x) * 3.51\ \mathrm{nm}(y) * 12.57\ \mathrm{nm}(z)$, and contains 33171 atoms. Periodic boundary conditions are applied on the dislocation line and glide directions, respectively. An embedded atom method (EAM) type potential [15] is employed. Atomistic modeling on dislocation-obstacle interactions at low strain rate (less than 10^6 s^{-1}) has been known as a challenge to molecular dynamics (MD) simulations [14]. Recently, a potential energy landscape (PEL)-based modeling framework combining the autonomous basin climbing (ABC) method and transition state theory (TST) has been proposed [16,17], which makes it possible to probe considerably lower strain rate conditions than in regular MD simulations. A schematic illustration of the modeling framework is shown in Fig. 1. At a given

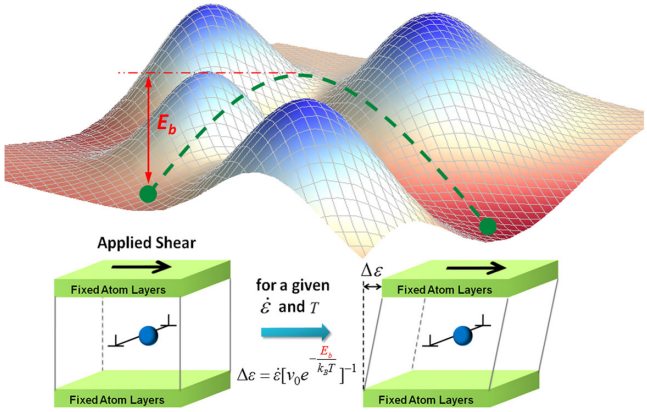

FIG. 1. Illustration for the dynamic model in capturing the dislocation-obstacle interaction as a function of strain rate $\dot{\varepsilon}$ and temperature T after combining the autonomous basin climbing method and transition state theory.

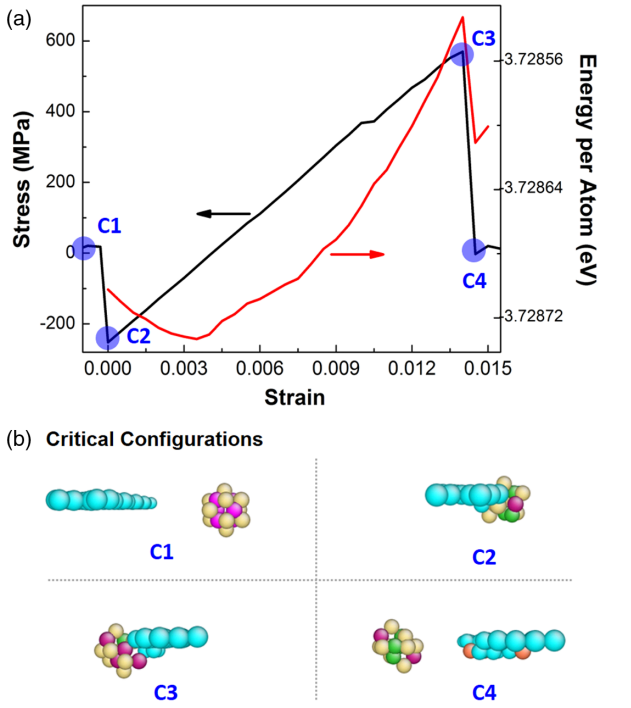

FIG. 2. (a) The stress-strain curve, and associated potential energy (per atom on average) of the system, during the static interaction. (b) Critical atomistic configurations during the static interaction as shown in (a). The atoms are visualized by Atomeye [20], and colored according to different coordinate numbers.

strain condition (including the initial state at zero strain), employ ABC to obtain the local dominant reaction pathway and associated activation barrier E_b in the system's underlying PEL. The corresponding thermal activation time at a given temperature can be calculated as $\Delta t = [\nu_0 e^{-\frac{E_b}{k_B T}}]^{-1}$, according to the TST, where ν_0 is the attempt frequency around 10^{13} s^{-1} [18]. For a specified strain rate $\dot{\varepsilon}$, the calculated strain increment, $\Delta\varepsilon = \dot{\varepsilon}\Delta t = \dot{\varepsilon}[\nu_0 e^{-\frac{E_b}{k_B T}}]^{-1}$, is then applied to the system. Keep doing the procedures iteratively until the dislocation is unpinned from the obstacle, one can then investigate the microstructural evolutions and associated stress-strain curves at prescribed strain rate and temperature.

To be more specific, a few atom layers near the top and the bottom (green regions) are set as rigid blocks in the simulation cell. The shear strain is implemented into the system by displacing the upper block as a whole [19]. At each strain state, the total force along the dislocation glide direction on the upper block F_b is calculated. The shear stress is then calculated as F_b/S_t, where S_t is the top surface area of the upper block. The CRSS is regarded as the peak stress of the stress-strain curve. More details of the model, in what we now call ABC-T, can be found in Refs. [16,17].

We first studied the interaction between the dislocation and the vacancy cluster under static conditions. Figure 2 shows the stress-strain curve, associated potential energy (per atom on average), and corresponding critical configurations.

In the beginning, the vacancy cluster is on the right side of the dislocation, with the center of mass placed on the glide plane. Upon shear loading, the dislocation is attached to the vacancy cluster [Fig. 2(b), C2] associated with a stress relaxation down to −251 MPa, indicating a very strong attractive pinning interaction in the early stage [14]. To better mimic the strain-controlled tensile test experimental condition, it is convenient to study the interaction as a function of strain. The corresponding strain at C2 is therefore set to be zero as a reference state. By further increasing the strain, there is a monotonic increase of the stress from C2 to C3. When the stress increases up to 570 MPa, the dislocation and vacancy cluster are detached from each other, leading to the sharp stress relaxation. The corresponding potential energy of the system during the interaction is also shown by the red curve in Fig. 2(a). Two vacancies in the void are absorbed by the dislocation during the static interaction, and a small jog is formed after the interaction [Fig. 2(b), C4].

We then probed the same interaction at room temperature and five different strain rates from 10^8 down to 10^3 s^{-1}, by employing ABC-T. The results are benchmarked against independent MD simulations at the high strain rates (10^6 and 10^8 s^{-1}), where MD is known to be valid. Figures 3(a)–3(b) show the corresponding stress-strain curves provided by ABC-T and MD simulation, respectively. It can be seen that all the CRSS at nonzero temperature are lower than the critical stress found in static calculation. It is also noticed that in the MD simulations [seen in Fig. 3(b)], the stress at the beginning is around −170 MPa, which is 80 MPa deviated from the static results [black curve in Fig. 3(a)]. We believe such a discrepancy is mainly attributed to the thermal compression stress produced in MD simulations, because of the fixed volume control (see Supplemental Material [21]). The atomistic configurations after the interactions are shown

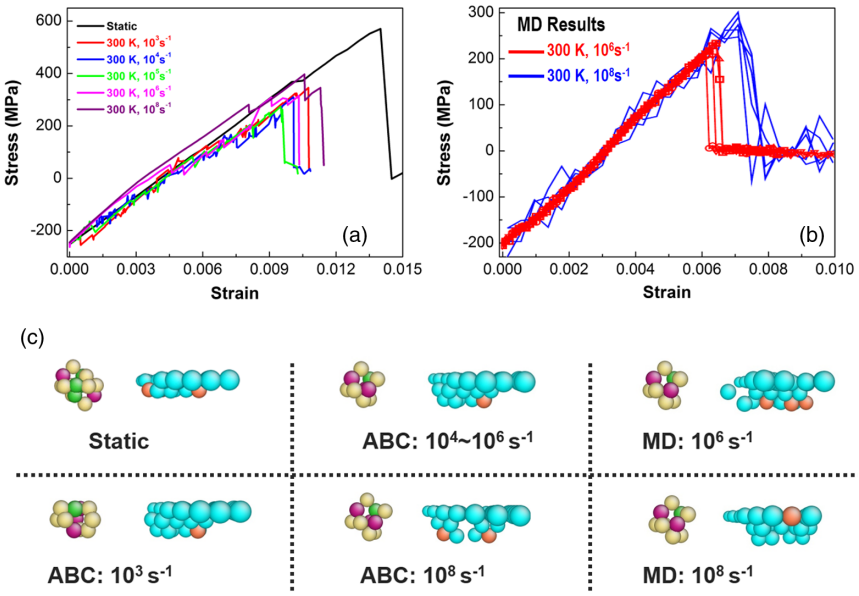

FIG. 3. (a)–(b) The stress-strain curves for the dislocation void interaction under different strain rate conditions, provided by ABC-T and MD simulations, respectively. (c) The associated critical atomic configurations after the interaction.

in Fig. 3(c). Compared to 2 vacancies being absorbed in static condition, 5 vacancies are absorbed by the dislocation under 300 K, while different strain rates lead to different atomic configurations after the interactions. In the ABC-T results, a most compact structure of the vacancy cluster is formed under 10^3 s^{-1}, as seen in Fig. 3(c). The remaining vacancy clusters for the strain rates between 10^4 and 10^8 s^{-1} are in the same structure, while the jogged dislocation at 10^8 s^{-1} has a relatively ripped structure because of the extremely high strain rate. As seen in Fig. 3(c), independent MD simulations show identical vacancy cluster configurations as in ABC-T results under the same conditions. The slight differences in dislocation structures are due to the atom oscillations in nonzero temperature MD simulations.

The CRSS under different strain rates are read off from Figs. 3(a)–3(b) and plotted in Fig. 4. According to the ABC-T results, for strain rates higher than 10^5 s^{-1} the CRSS increases as a function of strain rate, which shows a normal relation and is consistent with earlier studies [24,25]. It is noticed that under the same conditions, there are quantitative mismatches of CRSS between ABC-T and MD. The reasons could be twofold: (i) It might again originate from the thermal compression stress in MD simulations mentioned above; (ii) the attempt jump frequency ν_0 in ABC-T is set as 10^{13} s^{-1}. Although such value has been widely used and accepted, it might become larger upon strong entropy effects [26], which could lead to a lower CRSS because each strain increment step in the ABC-T simulation will be faster and the dislocation and the obstacle would detach from each other earlier.

More importantly, in spite of the quantitative mismatch, if one focuses on the net increases of CRSS from 10^6 to 10^8 s^{-1}, then clearly both ABC-T and MD studies show the same results. The agreements on the CRSS variations, along with the identical configurations shown in Fig. 3(c), demonstrate the robustness of the ABC-T algorithm in probing the dislocation-obstacle interactions.

Very interestingly, and surprisingly, the CRSS shows a nSRS behavior below 10^5 s^{-1} in ABC-T. To reveal the underpinnings of such phenomenon, we focus on the potential energy changes of the system during the evolutions, following the similar ideas proposed by Dutta *et al.* [27] and Monnet [28]. For each set of strain rate, a parabolalike shaped potential energy is observed, similarly as the red curve in Fig. 2(a). Figure 5(a) shows the energy differences at various strain rate conditions, with respect to the static interaction energy [red curve in Fig. 2(a)]. As seen in the figure, at relatively low strain rate 10^4 s^{-1}, there are more frequent fluctuations on the energy difference curve, indicating a significant amount of thermal activations and relaxations. For the higher stain rates such as 10^6 s^{-1}, the energy difference curve is smoother, which demonstrates the system is mainly driven by strain. It is worth noting that a similar serrate-smooth transition has also been observed in nanoindentation experiments, by increasing the applied strain rates [29].

The defect structure evolutions under different strain rates are shown in Fig. 5(b). At the early strain stage ($\varepsilon \sim 0.003$), the vacancy cluster is nucleated downward due to the thermal activation, for those strain rates between 10^3 and 10^5 s^{-1}. However, under high strain rates of 10^6 and 10^8 s^{-1}, no such nucleation is observed because there is not enough time for this event to be thermally activated.

Assisted by thermal activations, the dislocation core glides to the right side of vacancy cluster at medium strain stage [seen in Fig. 5(b), the configurations at $\varepsilon \sim 0.006$ for

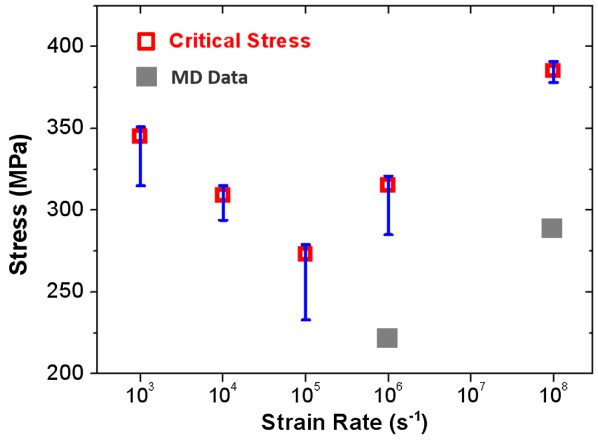

FIG. 4. The CRSS under different strain rate conditions. Red open squares are the results of ABC-T framework simulations, while the black squares represent the MD simulations results.

the strain rate between 10^3 and 10^6 s^{-1}]. This process is associated with the energy peak between $\varepsilon = 0.003$ and $\varepsilon = 0.006$ shown in Fig. 5(a). On the other hand, for the highest strain rate 10^8 s^{-1}, the dislocation does not glide to the right side of the vacancy cluster until the strain reaches the level around 0.009. This is because, at very high strain rate condition, the thermal activations are significantly suppressed and the similar interaction mechanism can only take place at deferred strain [16,30].

Upon further deformation, the structures of vacancy cluster show different evolutions at various conditions, as seen from S1–S5 in Fig. 5(b). Under the strain rates between 10^3 and 10^5 s^{-1}, the vacancy clusters show downward nucleation due to thermal activations [S1–S3 in Fig. 5(b)]. However, at 10^6 and 10^8 s^{-1}, the vacancy cluster is being ripped into parts [see S4 and S5 in Fig. 5(b)] rather than being nucleated, because there is not enough time for this event to be thermally activated at very high strain rates. The atomic density projection [14] along the x-axis (gliding direction of dislocation) shown in Fig. 5(c) also demonstrates a clear split behavior at high strain rates. It is worth noting that there are still strong connections between the ripped parts because their spatial spans are comparable with the cutoff radius of the EAM potential. Therefore, effectively the ripped structure at high strain rate imposes a larger surface area attaching to the dislocation core. At lower strain rate between 10^3 and 10^5 s^{-1}, the vacancy clusters nucleate to different structures (S1–S3). S1 and S2 are in a relatively looser structure than S3, and the lower energy minimum in the inset plot of Fig. 5(a) indicates that they are energetically more stable than S3. For both the loose structure (S1–S2) and the ripped structure (S4–S5), they have larger surface areas attached to the dislocation than S3 does. Correspondingly, the larger areas induce stronger impedances, and thus lead to higher critical

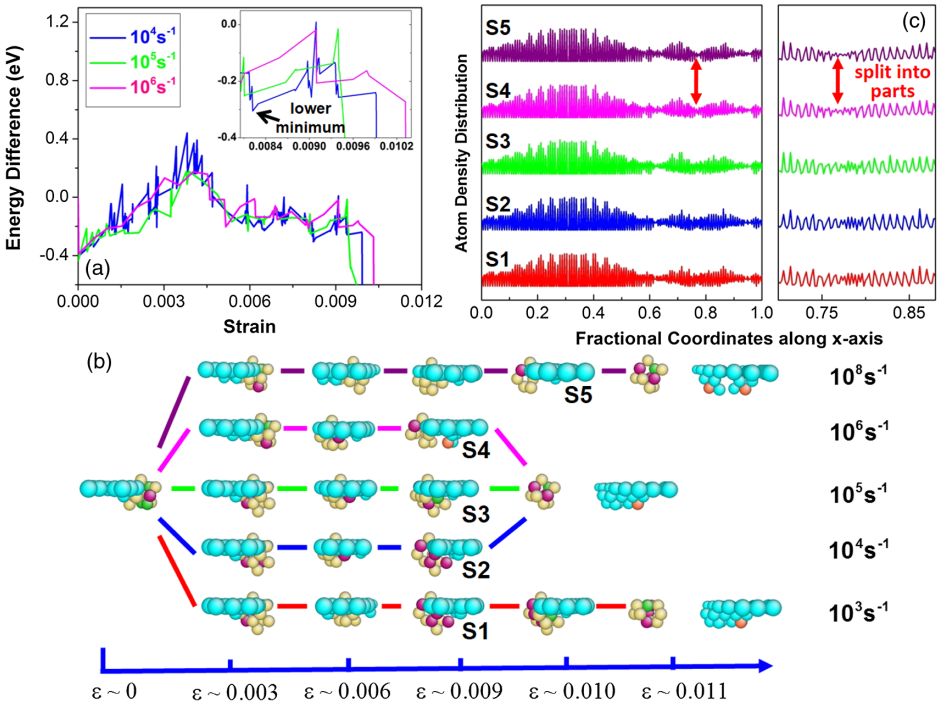

FIG. 5. (a) The potential energy differences of the system under different strain rate conditions, with respect to the static energy curve. (b) The atomistic configurations during the interactions, at various strain rates. (c) The atom density distributions along the x axis, i.e., the $\langle 111 \rangle$ direction, for structures S1–S5. The vacancy cluster's fractional coordinate along the x axis is about 0.8. It clearly shows that for high strain rates 10^6 and 10^8 s^{-1}, the vacancy clusters are ripped into parts, while such behavior is not observed for lower strain rates.

stresses. This explains the reason that the CRSS reaches its minimum at 10^5 s^{-1}.

By comparing the further evolutions between 10^3 and 10^4 s^{-1}, it can be found that the loose structure of vacancy cluster under 10^3 s^{-1} (S1) further nucleates to another stable configuration, because of more available time for thermal activation under lower strain rate. Subsequently, the stable structure leads to a higher CRSS than that in 10^4 s^{-1}. Therefore, in the entire simulated strain rate regime from 10^3 to 10^8 s^{-1}, the CRSS shows a "*V*" shape as seen in Fig. 4.

It is worth noting that the minimum strain rate considered here is 10^3 s^{-1}. In principle, the ABC-T method would allow us to tackle even slower processes. However, as illustrated in Fig. 1, at a given temperature too small strain rate can only implement a negligible strain increment during each iteration, which will tremendously increase the total computational costs. As a comparison, typical experiments concerning the dislocation-obstacle interactions are usually done in the strain rate regime between 10^0 and 10^{-3} s^{-1} [31–33], which seems still slower than the present study by several orders of magnitude. But we would like to note that such low rates usually refer to the global strain rates applied to the entire specimens in the mm order. And experiments [34,35] show that the deformation in the specimen is highly heterogeneous and largely localized within the so-called dislocation channels, of which the width is in the order of tens of nm. In other words, inside those channels where dislocation-obstacle interactions take place, the local strain rates can be up to 10^5 ($\sim$1 mm/10 nm) times larger than the average global strain rates. Since the present study focuses on the local dislocation-obstacle interaction, we therefore believe the hereby obtained results are not unrealistic.

In summary, we have examined a dislocation-vacancy cluster interaction in bcc Fe by a recently developed framework, ABC-T, which allows us to extend the atomistic modeling to low strain rate conditions. We demonstrate the dislocation-obstacle interaction is determined by two competitive factors: strain rate and thermal activation. Under low strain rates, thermal activations assist the vacancy cluster in nucleating to more stable states [S1 and S2 in Fig. 5(b)], which induces a stronger resistance to the dislocation and therefore lead to a higher CRSS than that in 10^5 s^{-1}. However, under high strain rates such as 10^6 and 10^8 s^{-1}, there is not enough time for the vacancy cluster nucleation being thermally activated. In contrast, the vacancy cluster is ripped to parts [S4 and S5 in Fig. 5(b)] due to the high strain rate. These parts impose a larger total area attached to the dislocation than the compact structure in 10^5 s^{-1} [S3 in Fig. 5(b)], which also leads to a stronger interaction with the dislocation and thus higher CRSS. All these together explain the underlying mechanism for the "*V*"-shape relation between CRSS and strain rate, with the minimum at 10^5 s^{-1}.

The inverse relation between CRSS and strain rate is known as the nSRS phenomenon, which could induce detrimental effects on the materials, such as the decreased ductility and strength, and the onset of mechanical instabilities [9,13]. Understanding and explaining such behavior are therefore critical for the material design strategies. In this work, we particularly examine the strain rate effects on the local interaction between a dislocation and a sessile obstacle. Through direct atomistic simulation we demonstrate that, in addition to the previously proposed global diffusion models [11–13], the local dislocation-obstacle interaction can also lead to the nSRS behavior.

We would like to stress that although the present study focuses on the nonmonotonic variation of CRSS in a bcc Fe system, the underlying principle—namely, the complex interplay between thermal activation and mechanical loading—is rather general and applicable to many different materials. For example, it has been found in a large variety of materials (including Al, Cu, Ni, Zr, and intermetallic $\gamma - \mathrm{TiAl}$) [16,17,36] that the microstructural evolutions of dislocations can be qualitatively different at different time scales. And the transitions between various mechanisms have been viewed as an underlying competition of strain rate and thermal activation, corroborating the spirit of the present study. As a final note, in addition to the strain rate effects probed in the present study, there are many other factors (e.g., system size, type of obstacle, etc.) could also affect the microstructural evolutions, which would warrant further studies in the future.

The authors acknowledge support from the U. S. Army Research Office Grant No. W911NF-18-1-0119. Y. F. is grateful to Bilge Yildiz, Akihiro Kushima, Sidney Yip, and Pradeep Sharma for helpful discussions.

*Corresponding author.
fanyue@umich.edu

[1] R. W. Grimes, R. J. Konings, and L. Edwards, Greater tolerance for nuclear materials, Nat. Mater. **7**, 683 (2008).
[2] V. Shastry and T. D. de la Rubia, The interaction between point defects and edge dislocation in bcc iron, J. Eng. Mater. Technol. **121**, 126 (1999).
[3] L. K. Mansur, Theory and experimental background on dimensional changes in irradiated alloys, J. Nucl. Mater. **216**, 97 (1994).
[4] G. S. Was, Materials degradation in fission reactors: lessons learned of relevance to fusion reactor systems, J. Nucl. Mater. **367–370**, 11 (2007).
[5] G. R. Odette, M. J. Alinger, and B. D. Wirth, Recent developments in irradiation-resistant steels, Annu. Rev. Mater. Res. **38**, 471 (2008).
[6] A. Kipelova, R. Kaibyshev, V. Skorobogatykh, and I. Schenkova, Portevin-Le Chatelier effect in an E911 creep resistant steel with 3%Co additives, J. Phys. Conf. Series **240**, 012100 (2010).

[7] M. A. Lebyodkin, Y. Brechet, Y. Estrin, and L. P. Kubin, Statistics of the Catastrophic Slip Events in the Portevin—Le Chatelier Effect, Phys. Rev. Lett. **74**, 4758 (1995).
[8] A. Bertram, T. Böhlke, C. Brüggemann, Y. Estrin, and M. Lebyodkin, Modeling and simulation of the Portevin-Le Chatellier effect, PAMM **6**, 353 (2006).
[9] J. M. Robinson and M. P. Shaw, Microstructural and mechanical influences on dynamic strain aging phenomena, Intl. Mater. Rev. **39**, 113 (1994).
[10] U. F. Kocks, A. S. Argon, and M. F. Ashby, in *Progress in Materials Science*, edited by B. Chalmers, J. W. Christian, and T. B. Massalski (Pergamon Press, New York, 1975), p. 110.
[11] Y. Brechet and Y. Estrin, On the influence of precipitation on the Portevin-Le Chatelier effect, Acta Metall. Mater. **43**, 955 (1995).
[12] S. Zhang, P. G. McCormick, and Y. Estrin, The morphology of Portevin–Le Chatelier bands: finite element simulation for Al–Mg–Si, Acta Mater. **49**, 1087 (2001).
[13] W. A. Curtin, D. L. Olmsted, and L. G. Hector, A predictive mechanism for dynamic strain ageing in aluminium–magnesium alloys, Nat. Mater. **5**, 875 (2006).
[14] D. J. Bacon, Y. N. Osetsky, and D. Rodney, in *Dislocations in Solids*, edited by J. P. Hirth and L. Kubin (Elsevier, New York, 2009), p. 1.
[15] G. J. Ackland, D. J. Bacon, A. F. Calder, and T. Harry, Computer simulation of point defect properties in dilute Fe—Cu alloy using a many-body interatomic potential, Philos. Mag. A **75**, 713 (1997).
[16] Y. Fan, Y. N. Osetskiy, S. Yip, and B. Yildiz, Mapping strain rate dependence of dislocation-defect interactions by atomistic simulations, Proc. Natl. Acad. Sci. U.S.A. **110**, 17756 (2013).
[17] X. Yan and P. Sharma, Time-Scaling in atomistics and the rate-dependent mechanical behavior of nanostructures, Nano Lett. **16**, 3487 (2016).
[18] A. F. Voter, in *Radiation Effects in Solids*, edited by K. E. Sickafus, E. A. Kotomin, and B. P. Uberuaga (Springer, Berlin, 2007), p. 1.
[19] Y. N. Osetsky, and D. J. Bacon, An atomic-level model for studying the dynamics of edge dislocations in metals, Model. Simul. Mater. Sci. Eng. **11**, 427 (2003).
[20] L. Ju, AtomEye: an efficient atomistic configuration viewer, Model. Simul. Mater. Sci. Eng. **11**, 173 (2003).
[21] See Supplemental Material at http://link.aps.org/supplemental/10.1103/PhysRevLett.120.125504 for the discrepancy between the ABC-T, and MD method due to the thermal compression stress, which includes Refs. [16,22,23].
[22] S. Alexander, Visualization and analysis of atomistic simulation data with OVITO–the Open Visualization Tool, Model. Simul. Mater. Sci. Eng. **18**, 015012 (2010).
[23] C. L. Kelchner, S. J. Plimpton, and J. C. Hamilton, Dislocation nucleation and defect structure during surface indentation, Phys. Rev. B **58**, 11085 (1998).
[24] D. Terentyev, L. Malerba, D. J. Bacon, and N. O. Yu, The effect of temperature and strain rate on the interaction between an edge dislocation and an interstitial dislocation loop in α-iron, J. Phys. Condens. Matter **19**, 456211 (2007).
[25] D. Terentyev, Y. N. Osetsky, and D. J. Bacon, Competing processes in reactions between an edge dislocation and dislocation loops in a body-centred cubic metal, Scr. Mater. **62**, 697 (2010).
[26] B. P. Uberuaga, R. G. Hoagland, A. F. Voter, and S. M. Valone, Direct Transformation of Vacancy Voids to Stacking Fault Tetrahedra, Phys. Rev. Lett. **99**, 135501 (2007).
[27] A. Dutta, M. Bhattacharya, N. Gayathri, G. C. Das, and P. Barat, The mechanism of climb in dislocation–nanovoid interaction, Acta Mater. **60**, 3789 (2012).
[28] G. Monnet, Mechanical and energetical analysis of molecular dynamics simulations of dislocation–defect interactions, Acta Mater. **55**, 5081 (2007).
[29] C. A. Schuh and T. G. Nieh, A survey of instrumented indentation studies on metallic glasses, J. Mater. Res. **19**, 46 (2004).
[30] Y. Fan, Y. N. Osetsky, S. Yip, and B. Yildiz, Onset Mechanism of Strain-Rate-Induced Flow Stress Upturn, Phys. Rev. Lett. **109**, 135503 (2012).
[31] F. Onimus and J.-L. Béchade, A polycrystalline modeling of the mechanical behavior of neutron irradiated zirconium alloys, J. Nucl. Mater. **384**, 163 (2009).
[32] F. Onimus, I. Monnet, J. L. Béchade, C. Prioul, and P. Pilvin, A statistical TEM investigation of dislocation channeling mechanism in neutron irradiated zirconium alloys, J. Nucl. Mater. **328**, 165 (2004).
[33] J. W. Dunlop, Y. J. M. Bréchet, L. Legras, and Y. Estrin, Dislocation density-based modelling of plastic deformation of Zircaloy-4, Mater. Sci. Eng. A **443**, 77 (2007).
[34] K. Farrell, T. S. Byun, and N. Hashimoto, Deformation mode maps for tensile deformation of neutron-irradiated structural alloys, J. Nucl. Mater. **335**, 471 (2004).
[35] N. Hashimoto, T. S. Byun, K. Farrell, and S. J. Zinkle, Deformation microstructure of neutron-irradiated pure polycrystalline metals, J. Nucl. Mater. **329–333**, 947 (2004).
[36] H. Wang, D. S. Xu, D. Rodney, P. Veyssière, and R. Yang, Atomistic investigation of the annihilation of non-screw dislocation dipoles in Al, Cu, Ni and γ-TiAl, Model. Simul. Mater. Sci. Eng. **21**, 025002 (2013).